

Differential Solute Gas Response in Ionic-Liquid-Based QCM Arrays: Elucidating Design Factors Responsible for Discriminative Explosive Gas Sensing

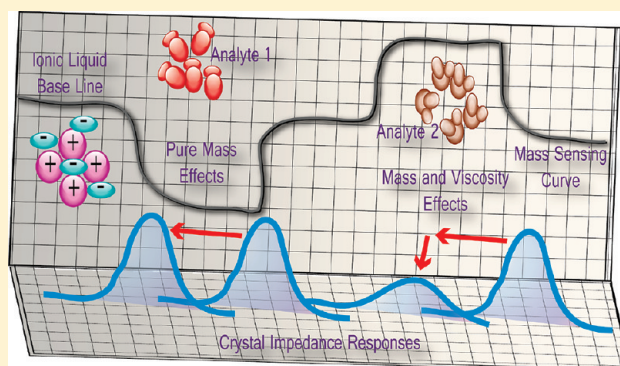
Abdul Rehman,[†] Andrew Hamilton,[†] Alfred Chung,[†] Gary A. Baker,[§] Zhe Wang,[†] and Xiangqun Zeng^{*,†}

[†]The Department of Chemistry, Oakland University, Rochester, Michigan 48309, United States

[§]The Department of Chemistry, University of Missouri—Columbia, Columbia, Missouri 65211, United States

S Supporting Information

ABSTRACT: An eight-sensor array coupling a chemoselective room-temperature ionic liquid (RTIL) with quartz crystal microbalance (QCM) transduction is presented in this work in order to demonstrate the power of this approach in differentiating closely related analytes in sensory devices. The underlying mechanism behind the specific sensory response was explored by (i) studying mass loading and viscoelasticity effects of the sensing layers, predominantly through variation in damping impedance, the combination of which determines the sensitivity; (ii) creation of a solvation model based on Abraham's solvation descriptors which reveals the fact that polarizability and lipophilicity are the main factors influencing the dissolution of gas analytes into the RTILs; and (iii) determination of enthalpy and entropy values for the studied interactions and comparison via a simulation model, which is also effective for pattern discrimination, in order to establish a foundation for the analytical scientist as well as inspiration for synthetic pathways and innovative research into next-generation sensory approaches. The reported sensors displayed an excellent sensitivity with detection limit of <0.2%, fast response and recovery, and a workable temperature range of 27–55 °C and even higher. Linear discriminant analysis (LDA) showed a discrimination accuracy of 86–92% for nitromethane and 1-ethyl-2-nitrobenzene, 71% for different mixtures of nitromethane, and 100% for these analytes when thermodynamic parameters were used as input data. We envisage applications to detecting other nitroaromatics and security-related gas targets, and high-temperature or real-time situations where manual access is restricted, opening up new horizons in chemical sensing.



The field of gas sensing possesses great room for innovative sensing materials capable of specific or selective interaction with various analytes of interest, because the available materials have their own limitations in performance. Considering the high specificity of biological receptors^{1,2} such as enzymes and antibodies, one naturally envisions their great potential to be used in biosensors, but most biorecognition elements cannot work under harsh real-world conditions³ and perish over time. Their artificial counterparts,⁴ on the other hand, are generally much more robust and long-lived but frequently suffer for want of better selectivity. For example, metal-oxide semiconductors,⁵ which are the most studied for gas sensing, are extremely nonspecific and rely heavily on data analysis tools in order to interpret results.^{6–8} For these reasons, organic recognition has attracted significant attention in recent years.^{9,10} When we talk about abiotic organic sensor elements, an appreciable diversity can be seen in the direction of designing¹¹ highly receptive and moldable materials,^{12–14} but yet again, key limitations include stability and sustainability, just as for biological sensors. Therefore, the key element for generating improved sensors, the

recognition element, remains of utmost importance. The need of the hour is to put forward innovative new materials that possess the flexibility of organics, the durability of inorganics, and the recognition selectivity of biomaterials, to make these devices part and parcel of our daily lives.

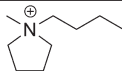
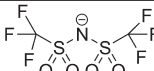
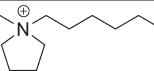
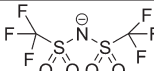
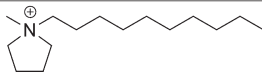
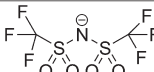
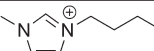
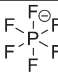
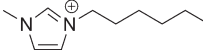
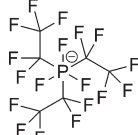
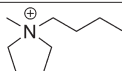
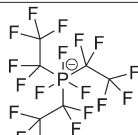
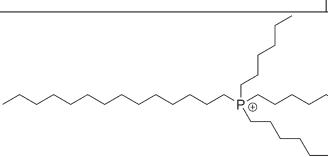
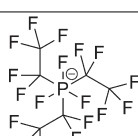
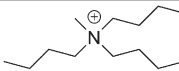
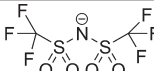
Room-temperature ionic liquids (RTILs)^{15–18} appear well-suited to this integrative approach, because of their special properties, although they remain relatively unexplored in the sensing field in which their potential is slowly being uncovered and disclosed.^{19–21} Being composed entirely of organic cations and anions, RTILs have a great synthetic flexibility which, in turn, provides enormous strength in fine-tuning their properties, especially in terms of their potential molecular interactions. Both ions are present in a fluidic environment, and show both independent and interactive ion functionalities, thus creating a complex, dynamic microenvironment characterized by ionic and

Received: June 21, 2011

Accepted: August 25, 2011

Published: August 25, 2011

Table 1. Room-Temperature Ionic Liquid (RTIL) Ion Structures and Thicknesses of Films Formed from Them

RTIL Abbreviation	Cation	Anion	Viscosity (cP)	Layer Thickness (nm)
[C ₄ mpy][NTf ₂]			56.3	297.46
[C ₆ mpy][NTf ₂]			87.6	386.40
[C ₁₀ mpy][NTf ₂]			136.6	363.77
[C ₄ mim][PF ₆]			270.3	191.35
[C ₆ mim][FAP]			317.4	189.68
[C ₄ mpy][FAP]			292	534.10
[P _{14,666}][FAP]			424.3	2180.35
[N _{444,1}][NTf ₂]			99.3	182.02

dipole forces, hydrogen bonding, and van der Waals interactions, on various time and space scales. This dependent variation on RTIL ionic composition and structure generates a criterion for selective incorporation and interaction with target analytes. In addition, great solvation ability of these molten salts enables the rapid and reversible incorporation of gases. The negligible vapor pressures and high thermal stabilities shown by RTILs are ideal for sensing purposes, especially in hazardous, high-temperature conditions by reducing the hazards associated with flash point and flammability seen for volatile organic compounds (VOCs). In sum, these features suggest the utilization of RTILs as an analyte-selective liquid membrane for signal transduction mechanism,²² a critical aspect in the development of low-cost sensors suited to mass production.

The bulk of the research involving RTILs is focused on their use as solvents^{23,24} for various reactions or stationary phases in a

variety of chromatographic separations;^{25–27} so naturally, the elucidation of their physiochemical behavior is primarily available in these areas^{28,29} or in the context of the pure components.³⁰ Despite the explanation required for these phenomena, it is equally important to gain insight into interactions when these materials are used as sensory materials, a flourishing topic in recent years. Specifically, a clear understanding is required, detailing how these materials behave when analyte molecules interact with them and the extent to which different forces come into play. Recently, we have published significant data establishing that RTIL/QCM (quartz crystal microbalance) architecture is ideally suited³¹ for the detection of VOCs as well as explosives, with interactions probed using vibrational spectroscopy. Often, the analyte/RTIL pairing primarily involves physical forces, rather than chemical ones, which require a detailed description. In some cases, the forces which significantly alter the properties

of the RTILs and hence are responsible for generation of sensing signals are predominantly nonbonding ones (e.g., polarizability, cavity formation effects), whereas hydrogen bonding and π -electronic cloud effects have a far less significant role to play. To substantiate this point, we present results on an array of QCM sensors coated with different RTIL thin layers which explain parameters of interaction, considering both thermodynamics and a solvation model for this class of sensors. We have included a range of RTILs in this study which differs in their sensing criteria in terms of viscosity and mass effects, differential temperature effects, and variability in sorption characteristics in order to draw more general, multidimensional conclusions. Optimistically, this innovation, on one hand, will help us to understand the molecular-level interactions within RTIL/QCM gas sensors and, on the other hand, it will open up new possibilities for the rational design of ion structures, leading to enhanced-performance sensors. After thoroughly investigating mass and viscosity effects, entropy and enthalpy values, and the solvation descriptors and their roles in defining the sensing model, we used these discriminative parameters to design an array of sensors that can be employed to distinguish different explosive mixtures with the help of a data analysis routine.

The analytes tested in this project included methane, nitromethane, and ethyl nitrobenzene (ENB). Methane, which is a major greenhouse gas, is a potential source of mine explosions when the composition of methane in air falls in the range of 5%–14%. Nitro compounds are a matter of concern for both environmental and security reasons, especially in the scenario of present terrorist activities. QCM was chosen as transduction platform,³² based on its facile readout mechanism, smart functionality, and above all, portability and miniaturizability,³³ which is essential for future commercial and field-portable instrumentation. A simple frequency measurement proportional to quantitative interactions of the sensor/analyte pair is adequate for detection as described by Sauerbrey's equation.

EXPERIMENTAL SECTION

Chemicals and Reagents. Nitromethane (CH_3NO_2) with >98.5% purity, and 1-ethyl-2-nitrobenzene ($\text{C}_8\text{H}_9\text{NO}_2$) with >98.0% purity were purchased from Sigma–Aldrich Co. Both analytes were used as received without further purification. Methane (99.99% purity) and nitrogen gas were purchased from Air Gas. RTILs used in this study were prepared by following reported methods^{34,35} and are listed in Table 1.

Sensor Preparation. Quartz crystals were purchased from International Crystal Manufacturing Company, Inc., with platinum (Pt) electrodes and a frequency of 10 MHz, while frequency monitoring was performed using a Maxtek RQCM quartz crystal microbalance research system. Pt was used as the electrode material, because its catalytic nature can enhance the interaction of thin films to the electrode surface, thus helping to form very stable sensing layers. Film thicknesses and other electronic properties of QCMs were monitored by the Agilent Model HP 4395A Network/Spectrum/Impedance Analyzer. For that purpose, QCMs were cleaned with deionized water and acetone and then dried under nitrogen to remove any contamination on the electrodes. RTIL solutions were made by dissolving the specific ionic liquid in ethanol (>99.5% purity) to form a solution with a concentration of 0.05 M. A micropipet was used to deposit 0.5 μL of the RTIL solution onto each side, at the center of the Pt sensor. Sensors were set in the gas chamber of the gas flow system and

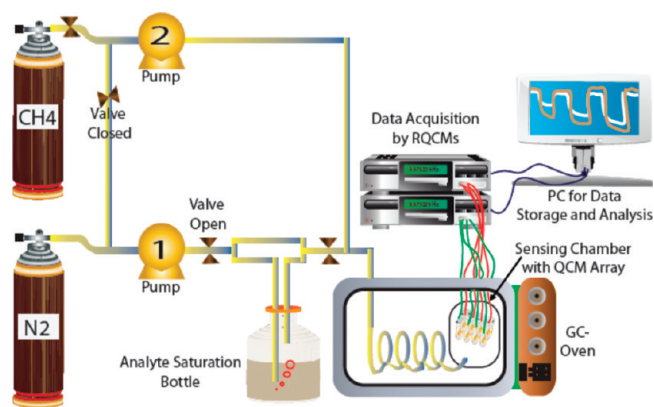


Figure 1. Setup for the flow and measurement in a gas sensor array.

allowed to dry at 55 °C with pure nitrogen flow. When the QCM reached a stable signal, the sensors were taken out and the new frequencies were measured. Ionic film thickness was calculated using the frequency shift with the help of Sauerbrey equation and taking into consideration the density of RTILs and the area of the electrodes, i.e., 0.23 cm^2 . Film thicknesses were in the range of 200–500 nm, with only $[\text{P}_{14,666}][\text{FAP}]$ resulting in a thickness outside this range. Film thickness is used to normalize the sensor responses in order to have better comparison of the data.

QCM Measurements. The gas flow system used to generate specified concentrations of target analytes was described in a prior publication.³⁶ Nitrogen gas was used as the carrying gas, whereas both methane and nitrogen were used as the diluting gas (as labeled in the experiments). Experiments were completed using two different total flow rates: 100 mL min^{-1} and 400 mL min^{-1} . The findings are not significantly different from the change of flow rate, except that the establishment of absorption–desorption equilibrium was more accomplished with lower flow rates, which is quite obvious, from a kinetics point of view. The slower flow rates allow more time for the molecules to interact with the absorbing materials, which, in turn, make them possible to have more interactions. That is the reason why we focused on the slower flow rate throughout the article. The concentration of the analyte was calculated using the ideal gas laws. A description of the setup is sketched in Figure 1. When methane was used as the diluting gas, the system shown describes the setup. When a stable baseline was being obtained and the analyte was “off,” pure nitrogen gas was driven through pump 2. When the analyte was turned “on,” nitrogen gas was redirected to pump 1 while pure methane flowed through pump 2. When one gas was driven through pump 2, the gas that was not in pump 2 was clamped at the indicated “X”. The diluted sample gas flowed through tubing, ~1 m in length, into the sensor chamber. The tubing and the sensor chamber were located in a gas chromatography (GC) oven, where the temperature was precisely controlled. The long pathway ensured homogeneous mixing of the sample vapor and the carrier gas, as well as the establishment of temperature equilibrium. The saturated sample gas was considered to be 100%. Concentrations of diluted vapors (expressed in terms of percentages) were calculated proportionately.

Data Analysis. Commercial SYSTAT12 statistics software (Systat Software, Inc., Chicago, IL) was employed to perform the classification of the different gas analytes. With this software, the frequency response of each analyte at different concentrations from the sensing array was converted to canonical variance

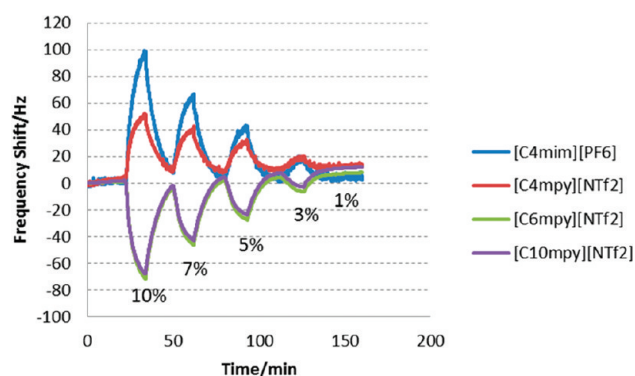


Figure 2. Response curves for four RTIL films against a flow of nitromethane at different concentrations in a nitrogen carrier gas.

from multidimensional space into two-dimensional coefficients, so that the distance can be calculated in multivariables and classified the distributions of different samples. The discriminant analysis is used to find a linear combination of the measures that best classifies or discriminates among the gas samples. The first two factor outcomes are the best discriminates among groups after linear combination calculation of the gas analytes by the linear discriminant analysis (LDA). In the canonical variable plot, the data plots aggregate within-group of the vapor class as cluster. Otherwise, data plots might separate into groups of different sample gases.

The same software package was used for the physiochemical analysis of the solvation process; but this time, multiple linear regression function was used and the calculated values are tabulated as required.

RESULTS AND DISCUSSION

Physical Insights into RTILs as Sensing Materials. *Mass Sensing Response Mechanism.* From the Sauerbrey equation, we know that the frequency changes proportionally with the mass. From initial experiments, it might be expected that, with the addition of the nitromethane, the frequency is going to decrease, because of the sorption process. With these specific analytes, however, this was not always witnessed. With the [C₄mpy][NTf₂] and [C₄mim][PF₆] sensor layers, the absorption of the nitromethane caused frequencies to increase. This is interesting because the [C₆mpy][NTf₂] and [C₁₀mpy][NTf₂] sensors had a decreasing frequency shift with the nitromethane, as shown in Figure 2. This result cannot be rationalized by the equation originally derived by Sauerbrey as mentioned below, which states that the change in frequency can be related to the change in mass, with some dependencies on the properties of the quartz. However, this equation is only valid if we assume that the increment of the foreign mass is uniformly distributed over the crystal surface with uniform density and the films behave rigidly.

$$\Delta f = -\frac{2f_0^2}{A\sqrt{\rho_q\mu_q}}\Delta m \quad (1)$$

Actually, a change in frequency in this type of nanogravimetric device is a function of the entire physiochemical environment of the media, rather than a mere mass effect. The density of the coated material, as well as the viscosity, play a key role in this regard. Kanazawa and Gordon³⁷ have extracted the expressions to treat the behavior of quartz crystals when they are exposed to liquid environments. When a crystal is dipped into a solution, the

oscillating frequency is dependent on the properties of that liquid. When an overlayer is thick, the relationship between Δf and Δm is no longer linear and corrections are necessary. The coupling of the crystal surface to a liquid drastically changes the frequency when a quartz crystal oscillates in contact with a liquid. The oscillation surface generates plane-laminar flow in the liquid, which causes a decrease in the frequency proportional to $(\rho_L\eta_L)^{1/2}$, where ρ_L and η_L represent the density and viscosity of the liquid, respectively. This leads to modification of the original Sauerbrey equation, in the form of eq 2:

$$\Delta f = -f_0^{3/2} \left(\frac{\eta_L \rho_L}{\pi \mu_Q \rho_Q} \right)^{1/2} \quad (2)$$

$$\delta = \left(\frac{\eta_L}{\pi f_0 \rho_L} \right)^{1/2} \quad (3)$$

where Δf is the frequency shift with the mass loadings, f_0 is the fundamental frequency of the QCM, and μ_Q and ρ_Q are elastic modulus and density of the quartz, respectively. In eq 3, δ is the decay length of the shear wave generated due to the oscillation of the quartz, and this is also related to both the density and the viscosity of the working fluid. The sorption of mass onto this film is directly related to the increase in density, which decreases frequency; but this may also cause a decrease in the viscosity of the ionic liquid layer. This decrease in viscosity reduces the damping effect, which can lead to increase of frequency. Therefore, eq 2 implies that the frequency of the QCM will change depending on the combined influences of density or viscosity of the sensing film due to their interactions with the analyte. Although the ionic liquids, because of their high viscosities, form stable layers just like the polymer matrices, the ion movement inside still retards them, to behave like rigid chemical entities, which is an obligatory requirement for the Sauerbrey equation. There is definitely some characteristic change that occurs when two carbons are added to the C4 chain of the alkylpyrrolidinium molecule, which makes the frequency shifts to occur in the completely opposite direction. These behavior can only be explained if we consider them as rigid liquids that retain their shape and stickiness, with the help of the above equations, as is done for classical liquids. The ongoing process of dissolution and removal of organic vapors causes the internal environment of the ionic liquids^{38,39} to change significantly, the most relevant of which is the viscosity change. Hussey^{40,41} and Seddon⁴² have carried out systematic studies to prove that the addition of low-viscosity solvents to different ionic liquids drastically change their viscosity and density, although the origin of this change is not fully rationalized. The most probable reason is the solvation of interacting anions and cations, which results in the decreased ion pairing and the aggregation, hence more distance among ions and more movement flexibility. Dai et al.⁴³ have quoted an example where, if you introduce the same amount of solvent to one ionic liquid and one polymer and calculate the frequency-shift values, using this equation (eq 2) and the Sauerbrey equation, respectively, you will get a positive shift of 1640 Hz for the IL and a negative shift of 250 Hz for a conventional polymer. If we assume this solvation of the contributing organic ions with the absorption of analytes to be correct, we can think of the limitless possibilities available where a large number of cations and anions can be variably combined to generate distinct solubility patterns toward various analytes. This phenomenon is used here, and a close

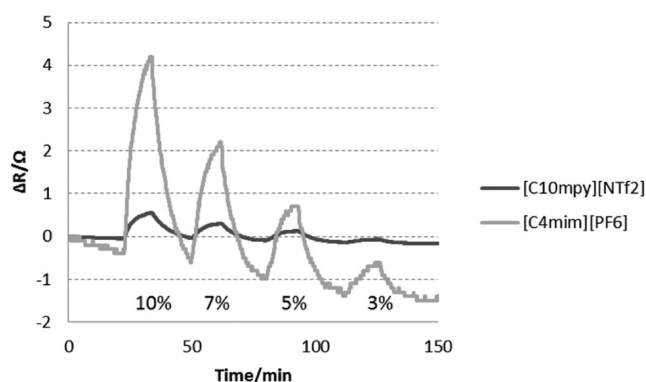


Figure 3. Variation of damping resistance during the binding events of nitromethane vapors onto RTIL layers.

examination of the curves in Figure 2 shows that, even if the frequency shift is in the same direction for two RTIL films, the amount of deviation is still different for all of them, which is due to both complementary and competing effects of viscosity and mass variations. Wherever the viscosity effect is more pronounced, we have an increase in frequency and we will refer to it here as a “positive shift”, and wherever the mass effect is more pronounced, the shift is in the normal direction and will be called a “negative shift”. Here, it can be clearly seen that $[C_6\text{mpy}][\text{NTf}_2]$ and $[C_{10}\text{mpy}][\text{NTf}_2]$ has a dominant mass effect, while $[C_4\text{mpy}][\text{NTf}_2]$, which belongs to the same class and differs only in chain length, has an opposite shift, because of the dominant viscosity effect. On the other hand, $[C_4\text{mim}][\text{PF}_6]$ showed even more of a positive shift than $[C_4\text{mpy}][\text{NTf}_2]$.

To better explain this competition of different physical values, we performed an acoustic impedance analysis, to characterize any energy loss or gain during the binding events. By determining the impedance or admittance spectrum in the vicinity of QCM oscillation resonance, and then by fitting through the Butterworth–Van Dyke circuit, the instrument can obtain the change in damping resistance over the entire measurement. Figure 3 plots the values of damping resistance of two of the RTILs, and a comparison of these plots with the frequency response curve clearly indicates that $[C_4\text{mim}][\text{PF}_6]$, which has dominant viscosity effects, shows a much larger damping change when the binding event has occurred. High resistance is a symbol of higher damping of crystal oscillation, which is a characteristic of a fluidic or viscoelastic material. Quite interestingly, the other RTIL also showed an increase in resistance, although it is a fraction of that shown by $[C_4\text{mim}][\text{PF}_6]$, but it helped us to explain two things. First, even RTILs with a positive frequency shift also show viscoelastic changes, and the total effect is viscogravimetric, because the earlier discussion suggests that RTIL layers should be considered as rigid liquid materials. Also, for those RTILs that demonstrate a very similar combined effect, e.g., $[C_6\text{mpy}]$ and $[C_{10}\text{mpy}]$, the shift in damping resistance for 10% of the analyte was 1.6 and 0.6 Ω , respectively, which means that their actual mass effects would have been different in the absence of these viscoelastic changes. Nevertheless, as we shall see, we were able to exploit these small variations in the behavior of RTILs sensing layers to discriminate very closely related explosive molecules.

Sensitivity Profile in Regard to Temperature. Temperature is another parameter that can possibly influence these sensing measurements significantly, for the following two reasons. First, if the temperature of the quartz crystal fluctuates, real mass

changes versus time measured greatly differ from the apparent mass changes, because of the temperature dependence of the quartz crystal. Consequently, the temperature dependence must be characterized and minimized to allow the QCM to provide an accurate monitoring.

In quartz crystal resonators, temperature dependence can be described by the following equation, as proposed in the work of Frerking:⁴⁴

$$\Delta f = a_1 f_0 (T - T_0) + a_2 f_0 (T - T_0)^2 + a_3 f_0 (T - T_0)^3 + \dots \quad (4)$$

where f is the frequency at any reference temperature T , and a_1 , a_2 , and a_3 are empirically determined constants that are related to the crystal orientation. For the AT-type quartz resonators that have been employed in this work, the frequency change is dominated by the a_1 and a_3 values. Consequently, the first derivative (df/dT) provides a frequency temperature dependence that is essentially quadratic, with respect to temperature. The local minimum is centered near room temperature and is typically negative in value. This produces two “crossover” temperatures that display zero frequency–temperature dependence. Typical AT-type resonators have relatively small frequency–temperature dependence over a large temperature range between -45°C and 90°C , which is normally $\sim 1\text{ Hz}/^\circ\text{C}$.

The second reason for temperature to be influential in this particular case is the changes in the RTILs, especially the viscosity change. This also is variably dependent on the structure and physical properties of the RTIL under study and is more visible in those that have pronounced viscosity effects during the mass adsorption process. Figure 4 presents some of the measurements done with two different RTILs and the bare platinum electrode to reveal these effects. For these measurements, each time, the baseline is achieved at the desired temperature and then a fixed concentration of nitromethane was allowed to pass across the sensors, thus generating a signal. As seen in the response curve, the bare platinum electrode showed no change in frequency at 27 and 35 $^\circ\text{C}$ and then there is an increase of $\sim 1.5\text{ Hz}$ per 1 $^\circ\text{C}$ rise in temperature. Also note that, for all of these temperatures, the sensor signals are almost the same, except for a slight decrease at 55 $^\circ\text{C}$. The $[C_{10}\text{mpy}][\text{NTf}_2]$ sensor, having a pronounced mass effect, also demonstrated that ability (i.e., when the temperature is varied from 27 $^\circ\text{C}$ to 45 $^\circ\text{C}$, it shows appreciably smaller frequency change but the sensor signal continued to be diminished with increasing temperature). In comparison to this, $[C_4\text{mim}][\text{PF}_6]$, which showed dominancy in viscosity effects, is drastically changing its baseline frequency with temperature fluctuations but yet again, the sensor signal continued to be diminished at higher temperatures, even though there is always a positive shift in this case, unlike that observed for $[C_{10}\text{mpy}][\text{NTf}_2]$, where there are negative shifts. This means that the analyte–RTIL interaction mechanism is also dependent on temperature; if this was not the case, the $[C_4\text{mim}][\text{PF}_6]$ sensor should have at least the same positive shift for analyte adsorption for all the temperatures in the background of the already-present positive viscosity effects due to the temperature. Therefore, regardless of whether the temperature produces viscosity shifts in the matrix of RTIL, it produces dynamic molecular changes, which reduce the interaction capabilities. The simplest explanation could be that the high thermal energy of the RTIL molecules enables them to have faster molecular motions, which, in turn, decline to accept the

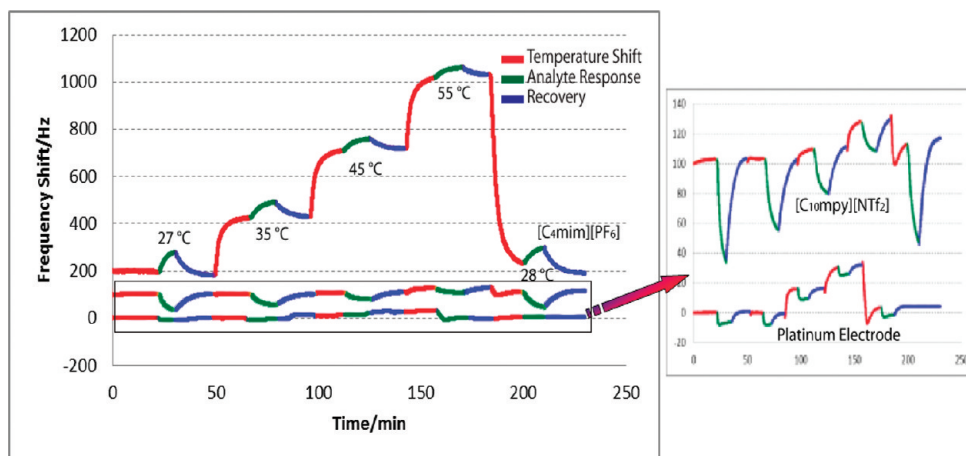


Figure 4. Response curves of bare platinum and RTIL-coated sensors with the variation of temperature when similar concentration of nitromethane is tested at a total flow rate of 100 mL min^{-1} .

interacting molecules. This is favored by the higher energies of gaseous analytes, thus pushing the adsorption–desorption equilibrium to be established at smaller frequency shifts.

Characterization of Sensors. Basic characteristics that are associated with quality sensors include their ability to show good sensitivity, discriminative selectivity (especially in the case when an array of sensors is being used), quick response, a wide range of linearity, and capability to demonstrate response and recovery in a reproducible manner. As shown in Figure 2, RTIL-based QCM sensors possess all these features, up to varying (but appreciable) extents. Sensitivity is quite remarkable, because only 1% of the concentration can generate visible effects and if the signal-to-noise ratio is taken as 3, the detection limit turns out to be $<0.2\%$ for all of the sensors. The sensitivity of these sensors can be increased by increasing the thickness of the RTIL coatings, as has been described in our previous work or use of the quartz crystal with higher fundamental frequencies;³⁶ but there are two important aspects that must be considered beforehand. First, when a very thin film is used, the frequency changes linearly, as a function of film thickness, but levels off after a threshold value. This value differs with the nature of RTIL and the analyte. This problem can be avoided by forming layers thin enough to have good linearity without compromising on the sensitivity. Second, it should also be noted that linear dependence of the frequency shift versus the mass loaded onto the quartz electrode is considered to be valid only if the shift is $<1\%$ of the fundamental frequency of the quartz used. This means that this limitation of Sauerbrey's equation, in this particular case, is 100 kHz (the fundamental frequency is 10 MHz). The implication of this requirement is significantly enhanced in the case of nonrigid systems such as RTILs with huge viscosity effects. This is why most of the sensors used in this study are coated with RTILs with a frequency effect of $\sim 10 \text{ kHz}$. Only the $[\text{P}_{14,666}][\text{FAP}]$ -coated sensor has a layer height of 71 kHz; therefore, before putting that sensor into actual testing, it has been tested for stability of signals, as well as the linearity of response, to ensure that the sensor behavior approximates that of a rigid system. The layer thickness data for the sensors used in this work are given in Table 1. Normalized calibration curves for eight RTIL sensors against four combinations of analytes in the concentration range of 1%–10% have been drawn, and the sensitivities have been calculated, as plotted in Figure 5. When ENB is used as analyte, all the sensors demonstrate a normal shift, which is described here as

positive, as shown in the figure. Here, all of the sensors except $[\text{C}_4\text{mpy}][\text{NTf}_2]$ and $[\text{P}_{14,666}][\text{FAP}]$ show appreciable sensitivity; however, the magnitude of response is quite different, even in the case of those RTILs that possess similar anions, which is very beneficial for developing sensor systems. Using nitromethane in place of ENB generated an entirely different pattern of responses, where $[\text{C}_4\text{mpy}][\text{NTf}_2]$ and $[\text{C}_4\text{mim}][\text{PF}_6]$ sensors exhibited negative shifts, which meant that, with this analyte, they have pronounced viscosity effects. On the other hand, $[\text{C}_6\text{mpy}][\text{NTf}_2]$ -, $[\text{C}_{10}\text{mpy}][\text{NTf}_2]$ -, and $[\text{C}_4\text{mpy}][\text{FAP}]$ -based sensors, which differ greatly in their sensitivity to ENB, have essentially an identical response pattern when nitromethane is flowed across them. This type of pattern formation is ideal to discriminate between different analytes. Continuing with the measurements, when we exposed the array to a mixture of ENB and nitromethane, we got a cumulative effect. The positive shifts in the case of nitromethane are enhanced, and the negative shifts are reduced with the addition of ENB as an analyte, which is quite expected, because all of the sensors showed a positive signal with pure ENB. When methane is used as the diluting gas, in place of nitrogen, the nitromethane effect is further enhanced, which also indicates that smaller molecules have a greater tendency to get solvated into the RTIL matrix, because they need less space between the interacting ions of the RTIL.

To explain the sensor response and recovery times, it is necessary to describe the kinetics of absorption and desorption phenomena, which can be represented by Figure 6. The rate of frequency shift is higher at the start and decreases with time, which can be associated with the equilibration of the solvation–desolvation process, as well as the dynamic behavior of the gaseous interactions usually associated with this type of sensor system. An important factor to mention here is that the response time shown here is a combination of time to saturate the sensing chamber as well as the tube network attached to MFCs on one side and to the chamber on the other side. The real response time is even smaller than the indicated one. Specifically to the working system here, after $\sim 10 \text{ min}$, the sensing films have already achieved a saturation of 85%–90%, which is adequate for two reasons. First, the rate of further reaction is too slow to achieve an absolute steady-state signal, because many time constraints are usually attached in real-life processes where high throughput is compulsory. In addition, for pattern recognition, a strict

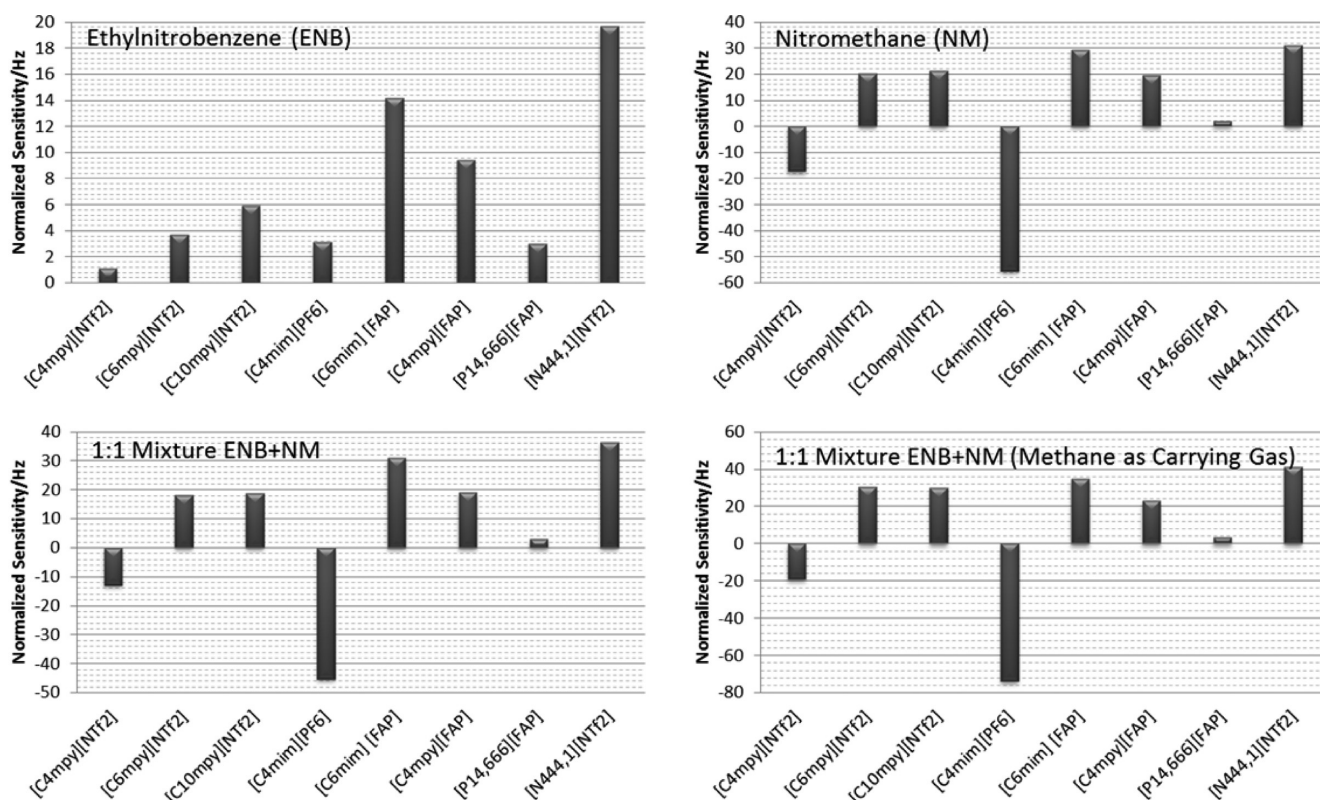


Figure 5. Sensitivity profile of analytes and their mixtures, as shown by the RTIL–QCM sensor array; the measurements are performed at room temperature, at a total flow rate of 100 mL min^{−1}. Data are normalized to a layer thickness of 1 μm for each RTIL and 1% of each analyte, and the sensitivities are calculated from actual calibration curves.

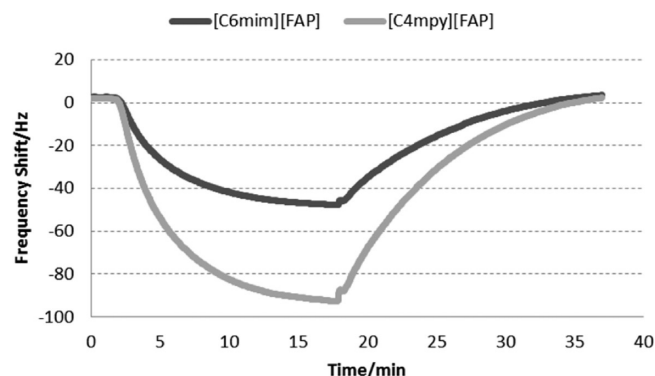


Figure 6. Real-time response curve for two different RTILs when nitromethane was flowing through the sensor cell, showing the solvation and desolvation process, as well as the response and recovery times.

obedience of signal calculation at specified time interval will eradicate the need for an absolute steady-state signal. As far as the recovery is concerned, it is slightly slower than the response. This indicates that the solvation of the analytes is a bulk process, rather than a surface process, and all the sublayers are responding to the analyte, thus, layer thickness is sufficient to standardize the sensor signals. This sensogram also depicts excellent recovery of the signal after going through the solvation–desolvation phenomenon, which eliminates the need of any special purging or washing system, thus reducing the complexity needed to employ the design for real-world applications. For calculation purposes, we waited at least 20 min for the recovery and then let

the next analyte into the process. We also investigated the recycling of the sensors over a long period of time with no significant loss of sensitivity, which is demonstrated in Figure S1 in the Supporting Information.

Physicochemical Treatment of the Solvation Process. The analysis of discriminative sorption characteristics for various RTILs toward the analytes of interest can be discussed in more specific physicochemical details with the help of a linear solvation energy relationship (LSER) method,^{46–48} which correlates the sorption process with molecular descriptors of sorbent and the sorbed species. For that purpose, the partition coefficient can be calculated from the frequency shifts in the system after coating of the RTIL and the saturation of the vapor by the following equation:

$$K = \Delta f_{\text{vap}} \left(\frac{\rho_{\text{IL}}}{\Delta f_{\text{IL}}} \right) M_{\text{vap}} C_{\text{vap}} \quad (5)$$

where K is the partition coefficient (the ratio of gas molecules outside and inside of the sorptive layer), Δf_{vap} the frequency shift when the sensor is fully saturated with the analyte, ρ_{IL} the density of RTIL, Δf_{IL} the layer height of the RTIL (in terms of frequency shifted while coating), M_{vap} the molar mass of the analyte, and C_{vap} the concentration of the analyte at which the saturation has taken place. Here, the partition coefficient is a sum of various parameters, where each parameter is a multiple of two individual parameters, each related to solute and the sorbent, and those are related to each other via eq 6:

$$\log K = c + eE + sS + aA + bB + vV \quad (6)$$

Table 2. Abraham's Solvation Descriptors for the Tested Analytes^a

gas analyte	<i>E</i>	<i>S</i>	<i>A</i>	<i>B</i>	<i>V</i>
nitromethane	0.313	0.95	0.06	0.31	0.4237
nitrobenzene	0.871	1.11	0	0.28	0.8906
methane	0	0	0	0	0.2495

^aData taken from ref 45.

Here, each parameter in the summation equation (except *c*) provides different strengths of both sorbent and the solute, respectively: *e* and *E* represent the ability to interact with each other's π - and n -electron pairs; *s* and *S* correspond to the measure of dipolarity and polarizability, respectively; *a* and *A* represent the complementary hydrogen bond acidity toward each other while *b* and *B* represent the complementary hydrogen bond basicity toward each other. Here, *v* is a combined term for the sorbent's cavity and dispersion interactions, whereas *V* is a symbol of Ostwald solubility coefficient of the solute, which is a measure of the dispersion/cavity factor or lipophilicity.

Table 2 provides the numeric values for these parameters of the analytes we tested. Here, one can observe that the factors related to the hydrogen bonding are nil for methane and very low for other two analytes, because their structures have no functionalities to form hydrogen bonds. Even methane has no ability to interact with the electronic structures of the solvent. This also was depicted in the multiple linear regression data, which we performed for various RTILs against the data for solute parameters. The calculated partition coefficients from the experimental data for each of the analyte/ionic liquid combination were used to perform the regression analysis through a commercially available protocol, to obtain the solvent descriptor values. After regression analysis, we only obtained nonzero values for *c*, *s*, and *v*, which are given in Table 3; this implies that hydrogen bond acidity, hydrogen bond basicity, and electronic cloud interactions have little to do with these RTIL–QCM-based sensors for explosives. The only terms that dictate the sensitivity are the polarization effect and the cavity/dispersion interactions. Different RTIL films possess varying strength of polarizability, and if we try to correlate this property, for example, with three [FAP]-based RTILs, it is observed that the higher the *s* value, the greater the interaction will be. Again, the cavity/dispersion factor is related the same way. The [N_{444,1}][NTf₂] sensor shows the highest response, although it has a much-lesser dispersion factor value than some of the other sensors, which, in our opinion, is due to the cumulative effect of both factors. This sensor possesses a very high ability to solvate the analyte, because of dipolarization, which is greatly enhanced, because of appreciably high cavity interactions. Thus, a combined effect is produced, leading to the highest response. Although [C₄mpy][NTf₂] and [C₄mim][PF₆] also possess high depolarization and cavity effects, they cannot produce responses as high as that of [N_{444,1}][NTf₂], because of the fact that their interaction with the analytes generates big viscosity changes, which causes fluctuation in LSER predictions. That is why the two sensors that show a big mismatch can be considered as outliers, because the basic assumption of the methodology is not fulfilled.

Thermodynamics of the Vapor-RTIL Interactions. Figure 7 describes the effect of temperature on the sensitivity of these RTIL-based sensors. The range of temperature used in this study covers almost all of the natural environment in which the

Table 3. Calculated Solvent Descriptors for RTILs Used with Multiple Linear Regression

RTIL	RTIL Solvation Parameters		
	<i>c</i>	<i>s</i>	<i>v</i>
[C ₄ mpy][NTf ₂]	−5.571	0.387	3.085
[C ₆ mpy][NTf ₂]	−5.022	−0.099	2.016
[C ₁₀ mpy][NTf ₂]	−5.022	−0.008	1.788
[C ₄ mim][PF ₆]	−5.048	0.350	3.362
[C ₆ mim][FAP]	−5.148	0.318	1.471
[C ₄ mpy][FAP]	−5.289	0.281	1.462
[P _{14,666}][FAP]	−6.009	0.075	0.300
[N _{444,1}][NTf ₂]	−5.166	0.406	1.327

prospected sensors have to work (i.e., 27–55 °C) without losing most of its sensing capability, which demonstrates the power of RTIL-based sensors, in comparison to routine polymer-based sensors. The decline of sensitivity is not linear in every case, so the sensors have not only maintained their selectivity toward various analytes, but the pattern formation also is enhanced by varying the degree of diminishing effect. Therefore, this factor also is able to play a role in the pattern recognition.

In order to standardize these effects, we calculated the adsorption enthalpy (ΔH) and adsorption entropy (ΔS) values from the data at different temperatures, using the van't Hoff's equations:

$$\Delta H = -R \left(\frac{\partial \ln x_i}{\partial T^{-1}} \right)_p \quad (7)$$

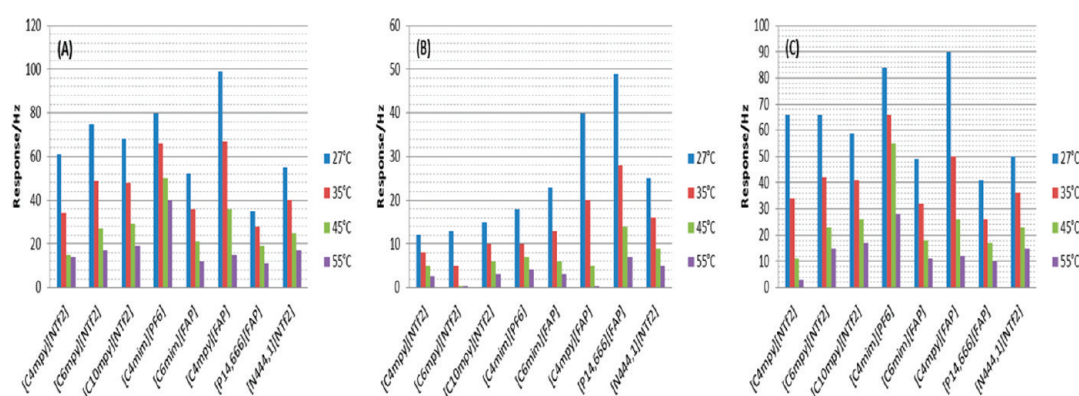
$$\Delta S = -R \left(\frac{\partial \ln x_i}{\partial \ln T} \right)_p \quad (8)$$

where x_i is the molar fraction of the gas dissolved in the RTIL, *T* the absolute temperature of the system, and *p* the partial pressure of the gas. Here, we have assumed that the molar fraction of analytes in the RTIL is very small. The $\ln x_i$ values are plotted against T^{-1} and $\ln T$, which showed very good linearity for all the RTILs. From the slope of these curves, the enthalpy and entropy for absorption in each RTIL for each analyte is calculated and compiled in Table 4.

Both of these measurements provide much information regarding the molecular interactions between the target analytes and the RTILs. Adsorption enthalpy values are related to the strength of the interactions, while entropy is useful in predicting the degree of molecular rearrangements during the solvation process. The total interactions are a function of both these properties, and a comparison of Table 4 with Figure 7 explains this idea. Here, it is seen that the response of the analyte will be higher if the energy of interaction is higher. The same is true for the entropy values, so when the entropy is higher, a variety of molecular rearrangements take place in order to facilitate the solvation of gas molecules. Especially in the case of ENB, where all the sensors are depicting gravimetric responses in large, we can find a direct relationship between sensitivities and these thermodynamic parameters. The same trend is observed with other analytes but with a difference for the sensors having significant viscosity effects, that it is not possible to clearly differentiate the molecular interactions from the viscosity changes. We have also tried to establish that these parameters are quite useful in

Table 4. Experimentally Calculated Values of Absorption Enthalpies and Absorption Entropies of Interaction for All Studied RTILs against the Target Analytes^a

RTIL	Enthalpy Values, ΔH_{ads} (kJ mol ⁻¹)			Entropy Values, ΔS_{ads} (kJ mol ⁻¹)		
	ENB	nitromethane	ENB + nitromethane	ENB	nitromethane	ENB + nitromethane
[C ₄ mpy][NTf ₂]	-19.83	-20.16	-31.95	-64.40	-65.33	-68.68
[C ₆ mpy][NTf ₂]	-30.39	-11.71	-11.74	-97.12	-37.41	-37.42
[C ₁₀ mpy][NTf ₂]	-14.65	-10.30	-12.34	-46.31	-32.91	-39.47
[C ₄ mim][PF ₆]	-11.45	-8.31	-18.40	-50.62	-26.50	-58.52
[C ₆ mim][FAP]	-34.13	-21.95	-27.24	-107.48	-68.80	-84.91
[C ₄ mpy][FAP]	-25.35	-11.27	-13.15	-53.57	-34.87	-41.29
[P _{14,666}][FAP]	-2.69	-1.61	-1.91	-8.40	-5.08	-5.89
[N _{444,1}][NTf ₂]	-27.87	-18.34	-25.11	-87.00	-57.58	-65.17

^a Each point is an average of two measurements.**Figure 7.** Diminishing of the effect with the rise of temperature for all the RTILs tested when the analytes used were (A) nitromethane, (B) ENB, and (C) a 1:1 mixture of nitromethane and ENB; the flow rate for these measurements was 100 mL min⁻¹.

determining the selectivity patterns and can enable us to generate the pattern recognition algorithm, which we will discuss under the Data Analysis section. Simulative modeling of these thermodynamic parameters is also performed using various models, which are discussed in the Supporting Information of this article.

Data Analysis. To ensure that the system (i) displays enough selectivity for our target analytes and (ii) is able to recognize them efficiently, we analyzed the data using linear discriminant analysis (LDA). For that purpose, steady-state datasets are extracted from the real-time measurements by averaging out the baseline signals obtained during the experiments. Each set represents eight signals each coming from one sensor. Before applying it to a commercially built LDA model from SYSTAT, the data are normalized to the thickness of the films. LDA is a means to attempt optimal class separation and seek the best class discriminatory information up to highest possible accuracy from a group of different variables. LDA is easy to maximize the ratio of intraclass variance, meanwhile minimizing the interclass variance for classification of data. That will help to perform an accurate classification of objects into groups according to the dependencies and connections among variables. There is a diverse set of data processing algorithms available but LDA is generally more useful than others, such as PCA in a system such as ours, because of its ability to transform the dataset to an easily controllable two-dimensional plot, and it also is a self-consistent method that is able to produce greater differentiation and less overlap between

groups. Therefore, other statistical algorithms are not demanded for our sensing system.

Figure 8 show the canonical score plots of first two factors with two different compilations of datasets and also the jack-knifed classification matrices obtained during the analysis. The basic idea behind the jack-knife variance estimation lies in systematically recomputing the statistical parameters, leaving out one or more data points at a time from the sample set. From this new replica of dataset, an estimate for the variance is calculated. The collection of classification data obtained in such a way is called a jack-knifed classification matrix. We have plotted only two factors, because >90% of the variance lies in these two. When the entire set of data is plotted, and three classes of analytes are separated from each other, there is an overall classification accuracy of 86%; however, the majority of the inaccuracy lies in differentiating nitromethane from the mixture, which is not discouraging at all, because, in the mixture, nitromethane has got a very high mass effect, which adds to the confusion matrix in overall discrimination. The second factor that came into our consideration is the fact that the sensors do not show absolute linearity at or below a concentration of 1%, which can be significant in classification. For this reason, we removed the 1% responses from the data and performed the data analysis again. This time, an accuracy of 92% is achieved with 100% classification for ENB. It is important to mention here that these datasets are for different concentrations of all the analytes, in contrast to most of the available sensor systems, where the classification is done for equal concentrations of

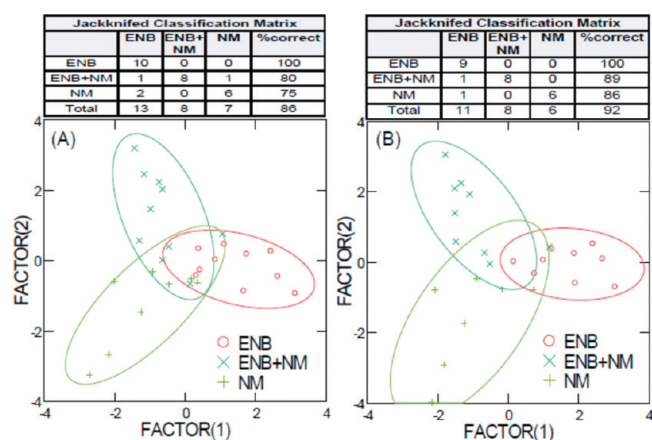


Figure 8. Canonical score plots and jack-knifed classification matrices for (A) the dataset as a whole and (B) the dataset not including 1% concentration responses.

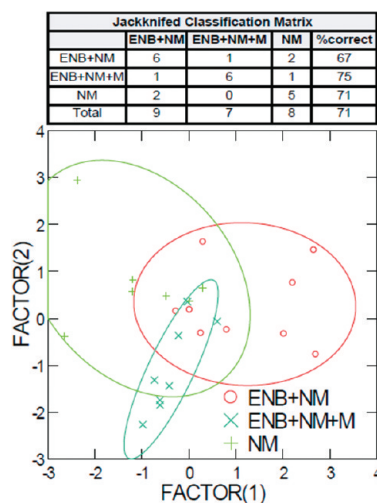


Figure 9. Canonical scores plot and jack-knifed classification matrix for the separation of nitromethane (NM) and its mixtures with ENB and methane (M).

analytes, which is quite innovative for our system, with regard to the capability of the RTIL-based sensors for selective detection. For another set of measurements, we collected the data from the same sensor array with nitromethane, a mixture of nitromethane and ENB, and the same mixture with methane as the carrying gas, and then we analyzed the data through LDA again. The results of this experiment are displayed in Figure 9. Even with this highly confusable dataset, we obtained an accuracy of 71%, which demonstrates the power of RTIL–QCM sensor arrays to differentiate between complex mixtures as well. Significantly enough, this type of system then can be used to build up a discriminative strategy that can be attached to a supervised algorithm, e.g., spiking neural networks, to define any analyte matrix quantitatively and to make decisions according to that definition.

As described in previous sections, thermodynamic parameters can also be used to classify these analytes, because they are clearly forming a pattern. To prove this point, the calculated interaction energies from the sensitivity plots are analyzed through LDA and the results obtained are given in Figure 10. Surprisingly, the

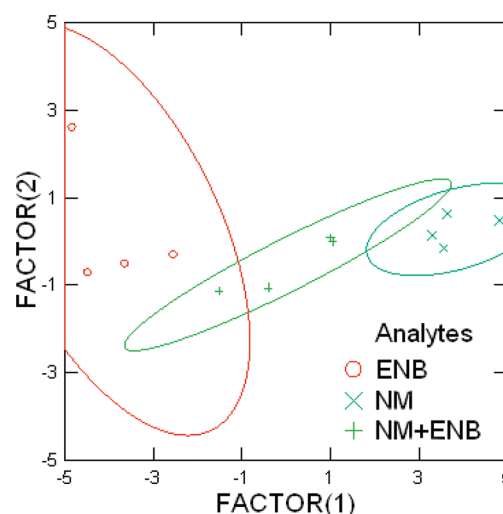


Figure 10. Data analysis plot when the data used consist of the interaction energies of the solvation, rather than actual sensor responses.

classification accuracy is 100% for all of the analytes. This is probably due to the fact that the thermodynamic factors have been calculated from the calibration curves and not the individual values, so the problematic nonlinearity in the response has been overcome. This means that precisely chosen RTIL–QCM sensors with selectivity toward some thermodynamic property can also solve various sensing problems.

CONCLUSIONS

Because of increasing use of room-temperature ionic liquids (RTILs) in different sensing applications, a physicochemical interpretation of the interaction forces involved in the sensing is highly required, which we have attempted to present in this publication. An array of eight self-synthesized RTILs coated onto Pt-based quartz crystal microbalance (QCM) sensors is used to identify the response mechanism with the help of different explosive materials in the gaseous phase as the test analytes, and different aspects of interaction chemistry are discussed. On one hand, the experiments proved that RTILs can be used as sensitive materials for a wide spectrum of applications, including modern-day security threats with appreciable selectivity and high throughput, while on the other hand, they have helped us to understand the basic parameters which determine this type of sensing. The solvation model that has been developed clearly defined that hydrogen bonding, as well as the electronic cloud interaction, have little to do with the sensing mechanism for this group of RTILs and the analytes—rather, the polarizability toward each other and cavity formation/dispersion effects dictate the interactive forces which can be a key factor in designing some new RTILs or their composites for future sensors. Thermodynamics of interactions also are calculated, and a comparison is done with modeled simulation, which turned out to be very similar, even with very simple assumptions. This hints that, by building a better model, a system of sensors can be designed, which has been tested for its recognition properties beforehand via simulative modeling. It is clearly seen that the response of the sensor is a combination of the effect of mass loaded and the viscoelastic fluctuations occurred during the sensing events, as validated by the damping resistance measurements, which is a significant factor in defining the selectivity toward projected detection candidates. Finally, the

array so proposed was tested for its discriminative power for very closely related explosive gases by the pattern recognition. The algorithm proved that the tested analytes are easily separable with appreciably low chances of error, and we are hopeful that this work can help us and others to understand the innovative nature of RTIL-based sensors and bring about many improvements in security-driven science.

■ ASSOCIATED CONTENT

S Supporting Information. The data for cycling and stability information and the simulation of thermodynamic parameters are available free of charge via the Internet at <http://pubs.acs.org>.

■ AUTHOR INFORMATION

Corresponding Author

*E-mail: zeng@oakland.edu.

■ ACKNOWLEDGMENT

We acknowledge an ONR grant (No. N000141010734) and support from Oakland University for this project. We like to thank Dr. Mike Sevilla's helpful discussion regarding quantum chemical calculations.

■ REFERENCES

- (1) Sommerhage, F.; Baumann, A.; Wrobel, G.; Ingebrandt, S.; Offenhausser, A. *Biosens. Bioelectron.* **2010**, *26*, 155.
- (2) Scheller, F. W.; Wollenberger, U.; Warsinke, A.; Lisdat, F. *Curr. Opin. Biotechnol.* **2001**, *12*, 35.
- (3) Gaster, R. S.; Hall, D. A.; Nielsen, C. H.; Osterfeld, S. J.; Yu, H.; Mach, K. E.; Wilson, R. J.; Murmann, B.; Liao, J. C.; Gambhir, S. S.; Wang, S. X. *Nat. Med.* **2009**, *15*, 1327.
- (4) Adhikari, B.; Majumdar, S. *Prog. Polym. Sci.* **2004**, *29*, 699.
- (5) Wang, C. X.; Yin, L. W.; Zhang, L. Y.; Xiang, D.; Gao, R. *Sensors* **2010**, *10*, 2088.
- (6) Vasiliev, R. B.; Ryabova, L. I.; Rummyantseva, M. N.; Gaskov, A. M. *Usp. Khimii.* **2004**, *73*, 1019.
- (7) Gardner, J. W. *Sens. Actuators B* **1991**, *4*, 109.
- (8) Sundgren, H.; Winquist, F.; Lukkari, I.; Lundstrom, I. *Meas. Sci. Technol.* **1991**, *2*, 464.
- (9) Crooks, R. M.; Ricco, A. J. *Acc. Chem. Res.* **1998**, *31*, 219.
- (10) Maldonado, S.; García-Berrios, E.; Woodka, M. D.; Bruntschwig, B. S.; Lewis, N. S. *Sens. Actuators, B* **2008**, *134*, 521.
- (11) Woodka, M. D.; Bruntschwig, B. S.; Lewis, N. S. *Langmuir* **2007**, *23*, 13232.
- (12) Dickert, F. L.; Haunschild, A. *Adv. Mater.* **1993**, *5*, 887.
- (13) Shao, Y. Y.; Wang, J.; Wu, H.; Liu, J.; Aksay, I. A.; Lin, Y. H. *Electroanalysis* **2010**, *22*, 1027.
- (14) Vairavapandian, D.; Vichchulada, P.; Lay, M. D. *Anal. Chim. Acta* **2008**, *626*, 119.
- (15) Buzzeo, M. C.; Hardacre, C.; Compton, R. G. *Anal. Chem.* **2004**, *76*, 4583.
- (16) Oter, O.; Ertekin, K.; Topkaya, D.; Alp, S. *Sens. Actuators, B* **2006**, *117*, 295.
- (17) Yu, L.; Huang, Y.; Jin, X.; Mason, A. J.; Zeng, X. *Sens. Actuators, B* **2009**, *140*, 363.
- (18) Seyama, M.; Iwasaki, Y.; Tate, A.; Sugimoto, I. *Chem. Mater.* **2006**, *18*, 2656.
- (19) Baker, G. A.; Baker, S. N.; Pandey, S.; Bright, F. V. *Analyst* **2005**, *130*, 800.
- (20) Tang, Y.; Baker, G. A.; Zeng, X. *J. Phys. Chem. C* **2010**, *114*, 13709.
- (21) Yung, K. Y.; Schadock-Hewitt, A. J.; Hunter, N. P.; Bright, F. V.; Baker, G. A. *Chem. Commun.* **2011**, *47*, 4775.
- (22) Yu, L.; Jin, X.; Zeng, X. *Langmuir* **2008**, *24*, 11631.
- (23) Rogers, R. D.; Seddon, K. R. *Science* **2003**, *302*, 792.
- (24) Chiappe, C.; Pieraccini, D. *J. Phys. Org. Chem.* **2005**, *18*, 275.
- (25) Anderson, J. L.; Armstrong, D. W. *Anal. Chem.* **2005**, *77*, 6453.
- (26) Qi, M.; Armstrong, D. *Anal. Bioanal. Chem.* **2007**, *388*, 889.
- (27) Wang, Q.; Baker, G. A.; Baker, S. N.; Colon, L. A. *Analyst* **2006**, *131*, 1000.
- (28) Heintz, A. J. *Chem. Thermodyn.* **2005**, *37*, S25.
- (29) Mutelet, F.; Jaubert, J.-N. *J. Chromatogr. A* **2006**, *1102*, 256.
- (30) Paulechka, Y. U.; Kabo, G. J.; Blokhin, A. V.; Shaplov, A. S.; Lozinskaya, E. I.; Vygodskii, Y. S. *J. Chem. Thermodyn.* **2007**, *39*, 158.
- (31) Hou, K.-Y.; Rehman, A.; Zeng, X. *Langmuir* **2011**, *27*, 5136.
- (32) O'Sullivan, C. K.; Guilbault, G. G. *Biosens. Bioelectron.* **1999**, *14*, 663.
- (33) Jin, X.; Huang, Y.; Mason, A.; Zeng, X. *Anal. Chem.* **2008**, *81*, 595.
- (34) Burrell, A. K.; Sesto, R. E. D.; Baker, S. N.; McCleskey, T. M.; Baker, G. A. *Green Chem.* **2007**, *9*, 449.
- (35) Kilaru, P.; Baker, G. A.; Scovazzo, P. J. *Chem. Eng. Data* **2007**, *52*, 2306.
- (36) Jin, X.; Yu, L.; Garcia, D.; Ren, R. X.; Zeng, X. *Anal. Chem.* **2006**, *78*, 6980.
- (37) Kanazawa, K. K.; Gordon, J. G. *Anal. Chim. Acta* **1985**, *175*, 99.
- (38) Moy, R.; Emmenegger, F.-P. *Electrochim. Acta* **1992**, *37*, 1061.
- (39) Fannin, A. A.; Floreani, D. A.; King, L. A.; Landers, J. S.; Piersma, B. J.; Stech, D. J.; Vaughn, R. L.; Wilkes, J. S.; Williams, J. L. *J. Phys. Chem.* **1984**, *88*, 2614.
- (40) Liao, Q.; Hussey, C. L. *J. Chem. Eng. Data* **1996**, *41*, 1126.
- (41) Perry, R. L.; Jones, K. M.; Scott, W. D.; Liao, Q.; Hussey, C. L. *J. Chem. Eng. Data* **1995**, *40*, 615.
- (42) Seddon, K. R.; Stark, A.; Torres, M. J. *Pure Appl. Chem.* **2000**, *72*, 2275.
- (43) Liang, C.; Yuan, C.-Y.; Warmack, R. J.; Barnes, C. E.; Dai, S. *Anal. Chem.* **2002**, *74*, 2172.
- (44) Frerking, M. E.; *Crystal Oscillator Design and Temperature Compensation*; Van Nostrand Reinhold Co.: New York, 1978.
- (45) Zissimos, A. M.; Abraham, M. H.; Klamt, A.; Eckert, F.; Wood, J. J. *Chem. Inform. Comput. Sci.* **2002**, *42*, 1320.
- (46) Abraham, M. H.; Zhao, Y. H. *J. Org. Chem.* **2004**, *69*, 4677.
- (47) Grubbs, L. M.; Acree, W. E.; Abraham, M. H. *Thermochim. Acta* **2010**, *509*, 87.
- (48) Torres-Lapasió, J. R.; García-Alvarez-Coque, M. C.; Rosés, M.; Bosch, E.; Zissimos, A. M.; Abraham, M. H. *Anal. Chim. Acta* **2004**, *515*, 209.